Project report for SCEC project: "Determination of Shallow Crustal Structure in Southern California and SCEC Community Model Validation Using Ambient-noise-derived Rayleigh Wave Ellipticity"

Abstract

A self-consistent regional-scale seismic velocity model with resolution from seismogenic depth to the surface is crucial for seismic hazard assessment. Though Southern California is the most seismically imaged region in the world, techniques with high near-surface sensitivity have been applied only in disparate local areas and have not been incorporated into a unified model with deeper resolution. In the present work, we obtain isotropic values for Rayleigh wave phase velocity and ellipticity in Southern California by cross-correlating daily time-series from the year 2015 across 315 regional stations in period ranges 6 to 18 seconds. Leveraging the complementary sensitivity of the two Rayleigh wave datasets, we combine H/V and phase velocity measurements to determine a new 3D shear velocity model in a Bayesian joint inversion framework. The new model has greatly improved shallow resolution compared to the SCEC CVMS4.26 reference model. Well-known large-scale features common to previous studies are resolved, including velocity contrasts across the San Andreas, San Jacinto, Garlock, and Elsinore faults, mid-crustal high-velocity structure beneath the Mojave Desert, and shallow Moho beneath the Salton Trough. Other prominent features that have previously only been imaged in focused local studies include the correct sedimentary thickness of the southern Central Valley, fold structure of the Ventura and Oak Ridge Anticlines, and velocity contrast across the Newport-Inglewood fault. The new shallow structure will greatly impact simulation-based studies of seismic hazard, especially in the near-surface low-velocity zones beneath densely populated areas like the Los Angeles, San Bernardino, and Ventura Basins.

Rayleigh wave H/V ratio

We use frequency-time analysis (FTAN; Bensen et al., 2007) to determine the maximum amplitude of the envelope for both causal and acausal sides of the ZZ, ZR, RZ and RR cross-correlations. Next, we measure H/V independently on both the causal and acausal portions of the correlograms. Specifically, for the first station (source station) we calculate H/V using RZ/ZZ and RR/ZR cross-correlation amplitude ratios for both the causal and acausal signals (i.e. four H/V measurements per station of each station pair). Similarly, for the second station (receiver station) H/V is determined using ZR/ZZ and RR/RZ cross-correlation amplitude ratios. We only retain good measurements by imposing several selection criteria, including signal-to-noise ratio greater than 5 and interstation distance larger than three wavelengths to satisfy the far-field condition (Bensen et al., 2007). For each period band, we define the signal-to-noise ratio as the average of the ratio of peak energy within the expected Rayleigh wave signal window, between 1.5km/s and 4.5km/s, to the root mean square of noise before and after the expected signal window (Lin et al., 2008). We apply this method to all cross-correlations to establish a large number of H/V measurements for each station.

We further stabilize each station's result in a quality control process designed to remove spurious measurements. We iteratively remove all measurements greater than three standard deviations, recomputing the mean and number of measurements within two standard deviations until no further measurements are discarded. For each station, we then use H/V measurements retained after stabilization to calculate isotropic H/V and uncertainty as the mean and standard deviation of the mean for each station, respectively.

Since H/V is a local measurement, we perform variable Gaussian smoothing to resolve log10(H/V) measurements throughout the entire region with 0.05º-by-0.05º spaced grid points setting the maximum Gaussian half-width as distance to the three nearest stations. To prevent overly-smoothed results, we discard any points within the region that do not have three stations within 50km. To propagate uncertainty, we determine the gaussian-weighted uncertainty from the standard deviation of the mean H/V of stations within the defined Gaussian distance for each grid point.

Monte Carlo 1D Inversion

By using a starting model that predicts the phase velocity dispersion fairly accurately, we are able to search the full model space and find a suite of best-fitting models to form the posterior. The starting model performs poorly at predicting H/V ratio. This is because the CVMS4.26 model (Lee et al., 2014) was developed using data with limited sensitivity to the shallow structure (e.g. the top 3 km). The inclusion of H/V data in the present work leads to strong changes in the shallow structure (<10km depth), which dramatically improves H/V fit in addition to slightly improving phase velocity fit. In nearly all cases, changes related to higher H/V in the data than the starting model correspond to low velocity zones in the upper few km that are completely absent in the starting model, especially near the Salton Trough, Coast Ranges and Indian Wells Valley. Because of the shallow sensitivity of the datasets, we do not constrain structure below ~25km depth; the posterior distributions are quite broad and simply average back to the starting model below this depth. Comparing prior and posterior model distributions indicates that the posterior models lie completely within the examined parameter space, are much more tightly constrained by the data than the prior distributions, and generally follow Gaussian distributions. In addition, the posterior distributions become wider with depth, indicating a relative decrease in model certainty as expected.
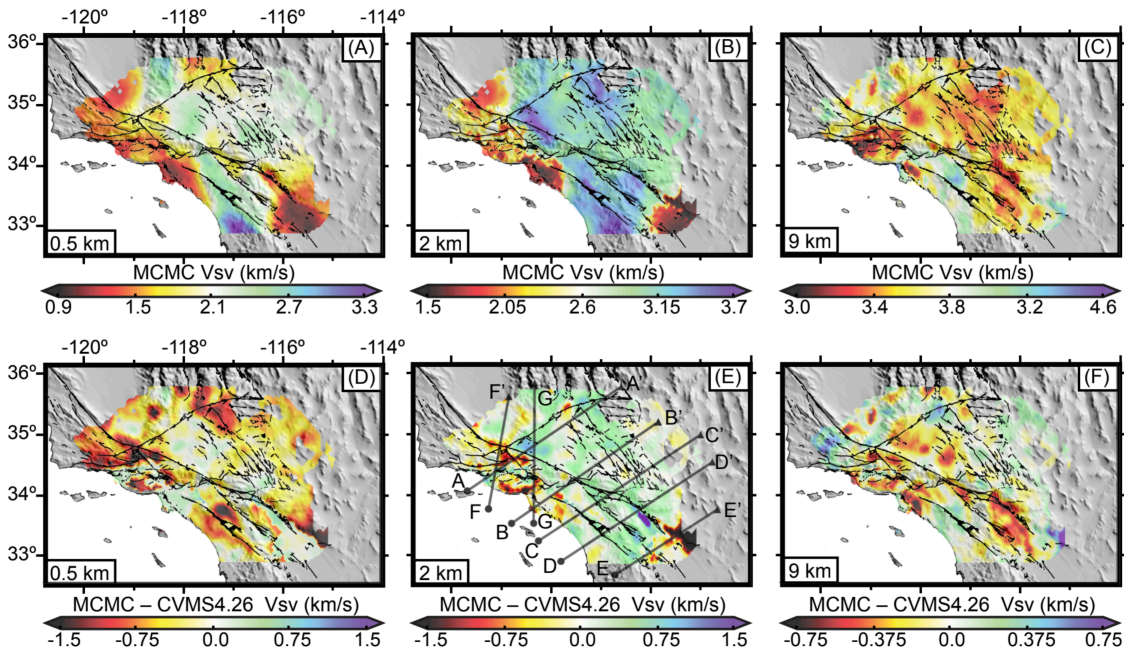
Figure 1. Joint inversion shear velocity (Vsv, km s^{-1}) results for depth of (a) 0.5 km, (b) 2 km, and (c) 9 km. Also shown are the differences between final and starting models for depths of (d) 0.5 km (e) 2 km (f) 9 km. Cross-sections denoted in (e) are shown in Figure 2.

Shear Velocity in 3D

The joint inversion results of Rayleigh wave H/V ratio and phase veolcity in terms of both absolute velocity and relative change to the starting model CVMS4.26 are presented in Figures 1 and 2. The map-view images have no smoothing applied after the individual 1D inversions, while the cross-sections were created using narrow-width cubic interpolation to sample along the arbitrarily-oriented profiles. The final model shows the strongest changes from the starting model at shallow depths due to the addition of H/V ratios in the inversion. These H/V data in general require lower velocities near the surface (<2km depth) and higher velocities in the upper crust compared to the starting model.

The final model improves fit of both phase velocity and H/V compared to the starting model. In general, misfit of the final model is low (< 1.5), except for the Los Angeles basin and in a few localized areas at the edges of the imaged region. This relatively high misfit in the LA basin is potentially due to the Moho being fixed at an incorrect depth in the present work; results from a recent dense seismic array indicate that the Moho beneath the LA basin is much shallower than previously thought (Ma & Clayton, 2016). Nevertheless, the new joint inversion model features significantly better fits to the data than the CVM-S starting model, including in the LA basin.

Conclusions

We combine Rayleigh-wave H/V ratios and phase velocity measurements in a joint Bayesian inversion to determine a regional shear velocity model for Southern California with improved resolution in the surface, shallow and upper crustal
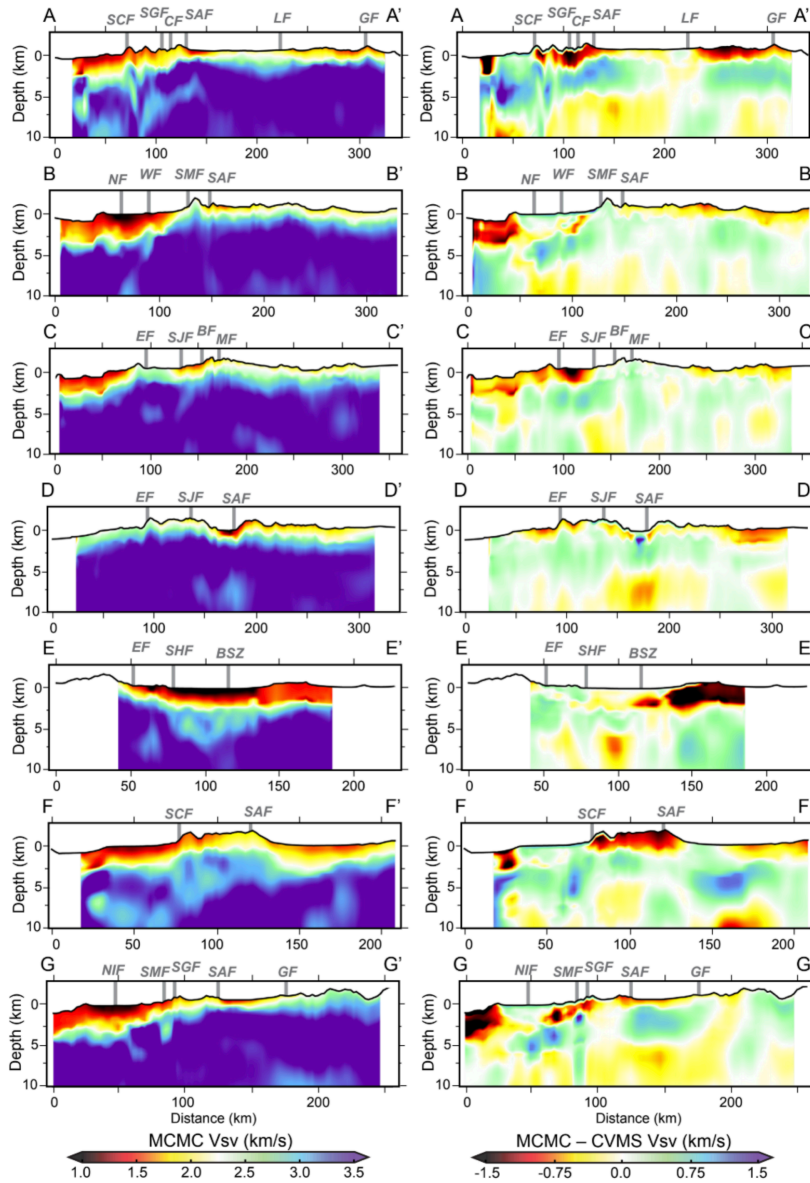
Figure 2. Cross-Sections (Figure 1e) of (left) final inversion Vsv results and (right) difference between final and initial (CVMS) Vsv. (a) A-A' cross section with the San Cayetano, San Gabriel, Clearwater, San Andreas, Lockhart and Garlock Fault surface traces marked. (b) B-B' cross-sections with the Newport-Inglewood, Whittier, Sierra Madre and San Andreas fault surface traces marked. (c) C-C' cross-sections with Elsinore, San Jacinto, Banning and Mill Creek fault surface traces marked. (d) D-D' cross-section with Elsinore, San Jacinto and San Andreas fault surface traces marked. (e) E-E' cross-section with Elsinore and Superstition Hills faults and Brawley seismic zone labeled. (f) F-F' cross-section with San Cayetano and San Andreas faults marked. (g) G-G' cross section with Newport-Inglewood, Sierra Madre, San Gabriel, San Andreas, and Garlock faults marked.

structure. Previous models such as the CVMS4.26 (Lee et al., 2014) have incorporated information from ambient noise and full waveforms but did not incorporate amplitude information and therefore have a relatively weak constraint on structure above 3km depth. By combining H/V ratios and phase velocity measurements, we gain sensitivity to shallow and mid-crustal shear velocity structure. The obtained large-scale mid-crustal features are similar to previous high-resolution models (e.g., Tape et al., 2010; Lee et al., 2014; Barak et al., 2015; Fang et al., 2016), lending confidence in the new model overall. The main improvement is the addition of new shallow features in the updated model, including more accurate basin depths and other near-surface low-velocity zones that have strong implications for studies of seismic hazard. The final model is a self-consistent regional-scale seismic velocity model with resolution from seismogenic depth to the surface.

In addition to resolving large-scale features of the crust, our shear velocity model includes small-scale shallow structure previously only seen by local imaging studies (Allam et al., 2014; Fliedner et al., 2000; Lin et al., 2013; Fuis et al., 2017). In the north this includes the shallower-sediments in the southern tip of the Central Valley (Fliedner et al., 2000; Fletcher & Erdem, 2017), high velocity of the Sierra Nevada Range (Tape et al., 2010), shallow slow velocities in the Coast and Transverse Ranges (Tape et al., 2010) and evidence of fold and thrust faults (Hubbard et al., 2014). We resolve similar shallow structure in the LA basin to the CVMS4.26 (Lee et al., 2014) while also imaging the Newport-Inglewood fault (Lin et al., 2013) and Whittier faults (Shaw and Suppe, 1996). We also are able to see the San Bernardino basin and differing velocity structure across the Elsinore, San Jacinto and San Andreas faults (Allam et al., 2014; Allam and Ben-Zion, 2012; Zigone et al., 2015). In the southern end of the region, we recover the Salton Trough and Peninsular Range with similar structure to active source studies (Livers et al., 2012; Fuis et al., 2017; Han et al., 2016). Our results demonstrate the considerable improvement to ambient noise imaging that can be gained from the incorporation of spatially dense Rayleigh wave H/V measurements to constrain shallow structure.

References

Allam, A.A., & Ben-Zion, Y. (2012). Seismic velocity structures in the southern California plateboundary environment from double-difference tomography. *Geophysical Journal International*, *190*, 1181-1196. https://doi.org/10.1111/j.1365-246X.2012.05544.x

Allam, A. A., Ben-Zion, Y., Kurzon, I., & Vernon, F. (2014). Seismic velocity structure in the Hot Springs and Trifurcation areas of the San Jacinto fault zone, California, from double-difference tomography. *Geophysical Journal International, 198(2),* 978–999. https://doi.org/10.1093/gji/ggu176

Barak, S., Klemperer, S. L., & Lawrence, J. F. (2015). San Andreas Fault dip, Peninsular Ranges mafic lower crust and partial melt in the Salton Trough, Southern California, from ambient-noise tomography. Geochemistry Geophysics Geosystems, 16, 3946-3972.

Bensen, G.D., Ritzwoller, M. H., Barmin, M. P., Levshin, A. L. , Lin, F., Moschetti, M. P., Shapiro, N. M. , & Yang, Y. (2007). Processing seismic ambient noise data to obtain reliable broad-band surface wave dispersion measurements. *Geophysical Journal International*, *169*(3), 1239–1260. https://doi.org/10.1111/j.1365-246X.2007.03374.x

Fang, H., Zhang, H., Yao, H., Allam, A., Zigone, D., Ben-Zion, Y., et al. (2016). A new algorithm for three-dimensional joint inversion of body wave and surface wave data and its application to the Southern California plate boundary region. Journal of Geophysical Research: Solid Earth, 121(5), 3557-3569. https://doi.org/10.1002/2015JB012702
Fletcher, J. B., & Erdem, J. (2017). Shear-wave Velocity Model from Rayleigh Wave Group Velocities Centered on the Sacramento/San Joaquin Delta. *Pure and Applied Geophysics*, *174*(10), 3825–3839. http://doi.org/10.1007/s00024-017-1587-x

Fliedner, M. M., Klemperer, S. L., & Christensen, N. I. (2000). Three-dimensional seismic model of the Sierra Nevada arc, California, and its implications for crustal and upper mantle composition. *Journal of Geophysical Research*, *105*(B5), 10899-10921. https://doi.org/10.1029/2000JB900029

Fuis, G. S., Bauer, K., Goldman, M. R., Ryberg, T., Langenheim, V. E., Scheirer, D. S., et al. (2017). Subsurface Geometry of the San Andreas Fault in Southern California: Results from the Salton Seismic Imaging Project (SSIP) and Strong Ground Motion Expectations. *Bulletin of the Seismological Society of America*, *107*(4), 1642–1662. https://doi.org/10.1785/0120160309

Han, L., Hole, J. A., Stock, J. M., Fuis, G. S., Kell, A., Driscoll, N.W, et al. (2016). Continental rupture and the creation of new crust in the Salton Trough rift, Southern California and northern Mexico: Results from the Salton Seismic Imaging Project. *Journal of Geophysical Research: Solid Earth*, *121*(10)*, 7469–7489. https://doi.org/10.1002/2016JB013139

Hubbard, J., Shaw, J. H., Dolan, J. F., Pratt, T. L., McAuliffe, L. J., & Rockwell, T. K. (2014). Structure and seismic hazard of the Ventura Avenue anticline and Ventura fault, California: Prospect for large, multisegment ruptures in the Western Transverse Ranges. *Bulletin of the Seismological Society of America*, *104*(3), 1070–1087. http://doi.org/10.1785/0120130125

Lee, E. J., Chen, P., Jordan, T. H., Maechling, P. B., Denolle, M. A., & Beroza, G. C. (2014). Full-3-D tomography for crustal structure in southern California based on the scattering-integral and the adjoint-waveform methods. Journal of Geophysical Research: Solid Earth, 119(8), 6421-6451. https://doi.org/10.1002/2014JB011346

Lin, F.-C., Moschetti, M. P., & Ritzwoller, M. H. (2008). Surface wave tomography of the western United States from ambient seismic noise: Rayleigh and Love wave phase velocity maps. *Geophysical Journal International, 173*, 281-298. https://doi.org/10.1111/j.1365-246X.2008.03720.x

Lin, F. C., Li, D., Clayton, R. W., & Hollis, D. (2013). High-resolution 3D shallow crustal structure in Long Beach, California: Application of ambient noise tomography on a dense seismic arrayNoise tomography with a dense array. *Geophysics*, *78*(4), Q45-Q56. https://doi.org/10.1190/geo2012-0453.1

Livers, A. J., Han, L., Delph, J., White-Gaynor, A., Petit, R., Hole, J. A., et al. (2012). Tomographic characteristics of the northern geothermally active rift zone of the Imperial Valley and its rift margins: Salton Seismic Imaging Project (SSIP). *AGU Fall Meet. Abstr*

Ma, Y. & Clayton, R.W (2016). Structure of the Los Angeles Basin from ambient noise and receiver functions. Geophysical Journal International, 206(3), 1645–1651. https://doi.org/10.1093/gji/ggw236

Shaw, J. H., & Suppe, J. (1996). Earthquake hazards of active blind-thrust faults under the central Los Angeles basin, California. *Journal of Geophysical Research: Solid Earth*, *101*(B4), 8623-8642. https://doi.org/10.1029/95JB03453

Tape, C., Liu, Q., Maggi, A., & Tromp, J. (2010). Seismic tomography of the southern California crust based on spectral-element and adjoint methods. Geophysical Journal International, 180(1), 433-462. https://doi.org/10.1111/j.1365-246X.2009.04429.x

Zigone, D., Ben-Zion, Y., Campillo, M., & Roux, P. (2015). Seismic tomography of the Southern California plate boundary region from noise-based Rayleigh and Love waves. *Pure and Applied Geophysics*, *172*(5), 1007-1032. https://doi.org/10.1007/s00024-014-0872-1